

This is a preprint of the following article, which is available at: <http://mdolab.engin.umich.edu>  
Anil Yildirim, Justin S. Gray, Charles A. Mader, and Joaquim R. R. A. Martins. Performance analysis of optimized STARC-ABL designs across the entire mission profile. *In Proceedings of the AIAA SciTech Forum*, January 2021.

The original article may differ from this preprint and is available at:  
<https://arc.aiaa.org/doi/10.2514/6.2021-0891>

# Performance Analysis of Optimized STARC-ABL Designs Across the Entire Mission Profile

Anil Yildirim

*Department of Aerospace Engineering,  
University of Michigan, Ann Arbor, MI 48109, USA*

Justin S. Gray

*NASA Glenn Research Center, Cleveland, OH, 44135, U.S.A.*

Charles A. Mader and Joaquim R. R. A. Martins

*Department of Aerospace Engineering,  
University of Michigan, Ann Arbor, MI 48109, USA*

## Abstract

Boundary layer ingestion (BLI) offers the potential for significant fuel burn reduction by exploiting strong aeropropulsive interactions. NASA's STARC-ABL concept uses an electrically powered BLI tail cone thruster on what is otherwise a conventional airframe. Despite this conventional airframe, aeropropulsive integration is critical to the performance of the BLI propulsor. In particular, the aeropropulsive integration of the BLI system must account for the variation in fan performance. Because it is electrically powered, the fan pressure ratio and efficiency of the BLI tail cone thruster vary widely across the flight envelope. Thus, accurate performance prediction for this novel propulsion configuration requires using a coupled aeropropulsive model across the flight envelope. In this work, we introduce a method to quantify the benefit of BLI at off-design conditions. We analyze the off-design performance of 18 optimized designs using an aeropropulsive model that is built with the OpenMDAO framework to couple 3-D RANS CFD simulations to 1-D thermodynamic cycle analyses. The designs are generated via high-fidelity aeropropulsive design optimizations for a range of fan pressure ratio and thrust values at the cruise conditions for the STARC-ABL concept. Performance analyses are then performed at a range of off-design flight conditions that

span the flight envelope, including low-speed and low-altitude flight conditions. This study provides the first set of high-fidelity data for the STARC-ABL configuration at off-design conditions. The results quantify the power savings through BLI compared to a traditional propulsion system across the entire mission profile. Finally, the results and techniques from this study will guide the extension of current aeropropulsive design capabilities to multipoint design optimizations.

## 1 Introduction

Boundary layer ingestion (BLI) is a concept where a propulsion system ingests the boundary layer generated by the airframe to improve the aeropropulsive performance of the aircraft [1]. While the concept is not new, BLI technology has not been utilized in a practical aircraft configuration because BLI system design is challenging [2], and traditional design tools fall short of capturing the coupled aeropropulsive effects. Furthermore, traditional thrust and drag accounting approaches cannot be used for BLI configurations because the propulsion system is tightly integrated with the airframe [3]. As a result of these challenges, various bookkeeping approaches have been developed to quantify the effects of BLI. Habermann et al. [4] reviews these methods and tries to develop a unified approach that is applicable to a wide range of configurations. Similarly, there has been a wide range of approaches to model systems that use BLI. Hendricks [5] reviews these efforts at NASA and lists design approaches with a range of model fidelities and degrees of coupling. Furthermore, Menegozzo and Benini [6] review the modeling approaches used in studies of aircraft configurations that use BLI.

To quantify the benefits of BLI on a configuration, Smith [7] proposed a power-based metric called power saving coefficient (PSC), defined as

$$\text{PSC} = \frac{\mathcal{P}_{\text{shaft}} - \mathcal{P}_{\text{shaft-BLI}}}{\mathcal{P}_{\text{shaft}}} . \quad (1)$$

This metric represents the reduction in the power requirements for a configuration utilizing BLI ( $\mathcal{P}_{\text{shaft-BLI}}$ ) compared to a reference podded configuration ( $\mathcal{P}_{\text{shaft}}$ ) to achieve the same net force coefficient on the overall body. This is a convenient metric because it side-steps the challenges with force-based accounting [3, 8]. Therefore, we use PSC as the figure of merit that quantifies the benefit of BLI.

A promising configuration that uses BLI is the STARC-ABL concept introduced by NASA [9], where a propulsor mounted on the tail cone of a conventional tube and wing configuration is used to ingest the boundary layer generated by the fuselage to improve aeropropulsive performance, as visualized in Figure 1. Based on the aeropropulsive design framework developed by Gray et al. [10], we performed aeropropulsive design optimizations of the STARC-ABL configuration at a range of fan pressure ratio (FPR) values and fan sizes. This resulted in 9 optimized STARC-ABL designs that quantify the power requirement of the BLI fan [11]. Following this study, the authors performed an additional set of optimizations that quantify the power requirement of both the BLI and a podded reference configuration to quantify the PSC values of the STARC-ABL concept at a range of FPR values and fan sizes, resulting in a total of 18 optimized

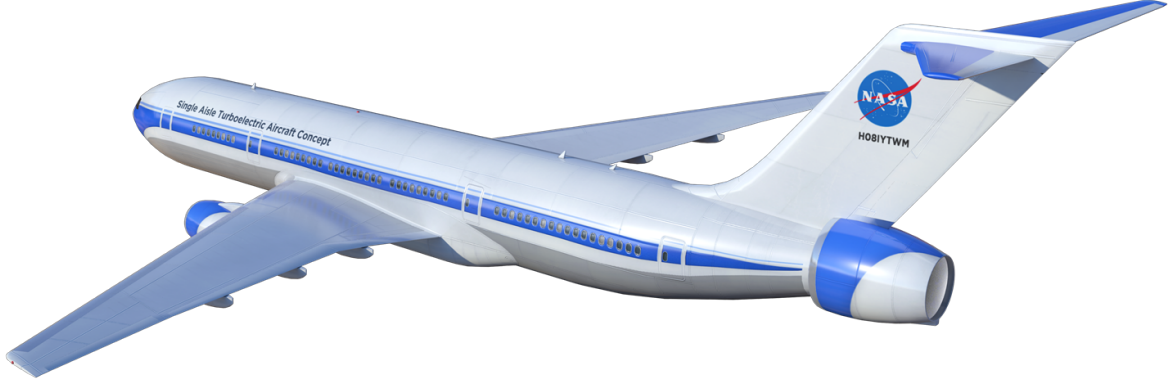


Figure 1: Rendering of the STARC-ABL configuration. The electric tail-cone thruster ingests the fuselage boundary layer to improve aeropropulsive performance.

designs [12]. While these studies quantified the performance benefits of BLI on the STARC-ABL configuration, these benefits were analyzed only at cruise conditions, which was chosen as the design point for the BLI fan. However, a typical mission of the STARC-ABL concept involves a range of flight conditions. The benefits of BLI must also be estimated at these *off-design* conditions to compute the total energy savings from BLI.

In this work, we analyze the aeropropulsive benefits of BLI on the STARC-ABL concept at a range of off-design flight conditions. For this study, we use the 18 optimized designs from [12], and analyze the aeropropulsive performance at 9 operating conditions. Using these results, we compute the PSC values at these operating conditions and study PSC values' sensitivity to various flight parameters. Besides guiding future studies on the required coupling level to predict aeropropulsive performance at various flight conditions, these results will be the first set of high-fidelity performance data for the STARC-ABL configuration across the mission profile.

The outline of the paper is as follows. Section 2 describes the coupled aeropropulsive models of the BLI and podded configurations of the STARC-ABL concept, and Section 3 summarizes the results of 18 optimized designs from our previous work [12]. Then, Section 4 introduces our off-design analysis methodology, and Section 5 lists the results from this study, followed by the conclusions in Section 6.

## 2 Coupled Aeropropulsive Model

The coupled aeropropulsive design framework we use in this work is based on the previous work by Gray et al. [10] and current authors [11, 12]. The geometry is modeled using OpenVSP<sup>1</sup> [13], and the mesh warping is performed using the IDWarp package<sup>2</sup> [14]. The aeropropulsive model consists of 3-dimensional RANS CFD to model the aerodynamics, and a 1-dimensional propulsion cycle analysis to estimate the shaft-

<sup>1</sup><https://github.com/OpenVSP/OpenVSP>, accessed November 2020

<sup>2</sup><https://github.com/mdolab/idwarp>, accessed November 2020

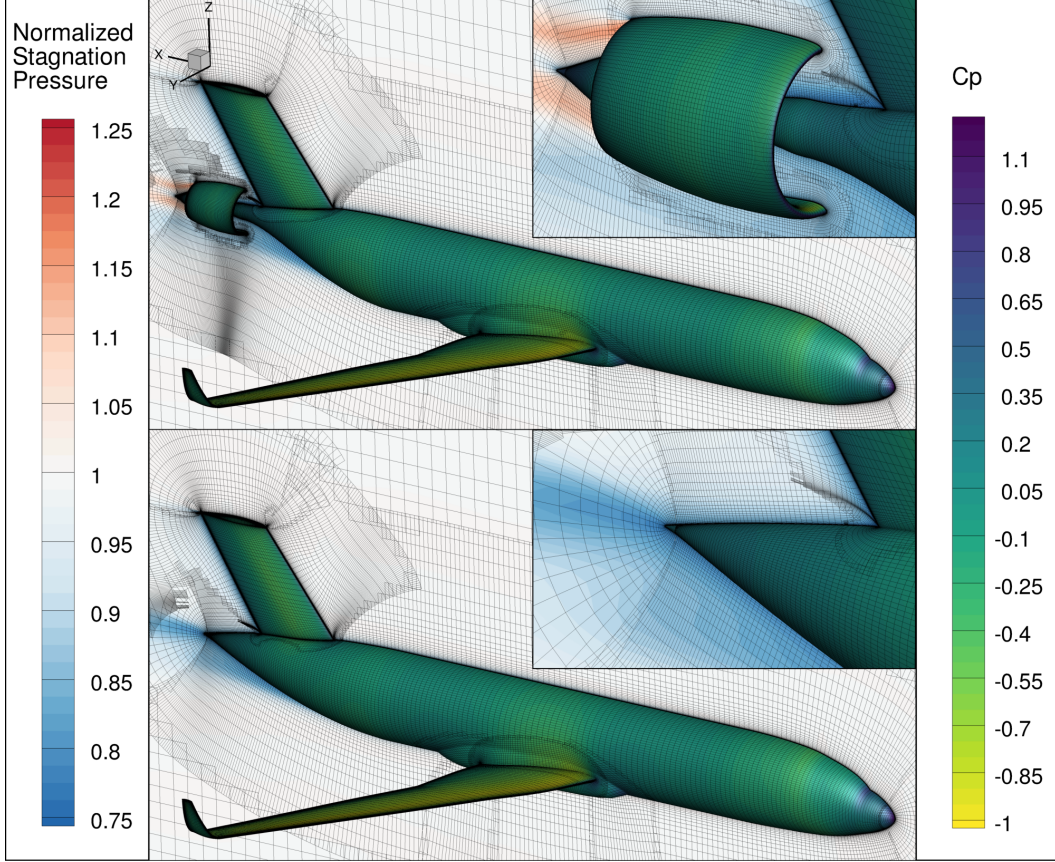


Figure 2: CFD solutions of the BLI (top) and non-BLI (bottom) configurations. Details of the tail-cone are shown on the upper-right corner of each figure.

power requirements of the fan. We use ADflow<sup>3</sup> [15] as the CFD solver, and a simple fan model built with the pyCycle package<sup>4</sup> [16]. In this work, we use the approximate Newton–Krylov solver in ADflow to converge the CFD simulations [17], along with the efficient adjoint implementation in ADflow to obtain accurate gradients [18]. The aerodynamic and propulsion models are coupled using the OpenMDAO framework<sup>5</sup> [19], which is also used to solve the coupled derivative problem.

For the BLI configuration, we have a single CFD model that analyzes the integrated airframe-BLI fan system, as shown in the top half of Figure 2. Besides the BLI configuration, we also analyze a reference podded configuration, where the BLI fan is not integrated to the airframe, and is modeled as a podded fan that ingests free stream air. For this configuration, we analyze the reference airframe separately from the podded fan, as shown in the bottom half of Figure 2. Besides this, we also have a separate CFD mesh that is used to model the podded fan at free stream conditions, as shown in Figure 3. With these two models, we can perform two sets of analyses for each optimized design, which is required to obtain the PSC value (Eq. 1) at each flight

<sup>3</sup><https://github.com/mdolab/adflow>, accessed November 2020

<sup>4</sup><https://github.com/OpenMDAO/pyCycle>, accessed November 2020

<sup>5</sup><https://github.com/OpenMDAO/OpenMDAO>, accessed November 2020



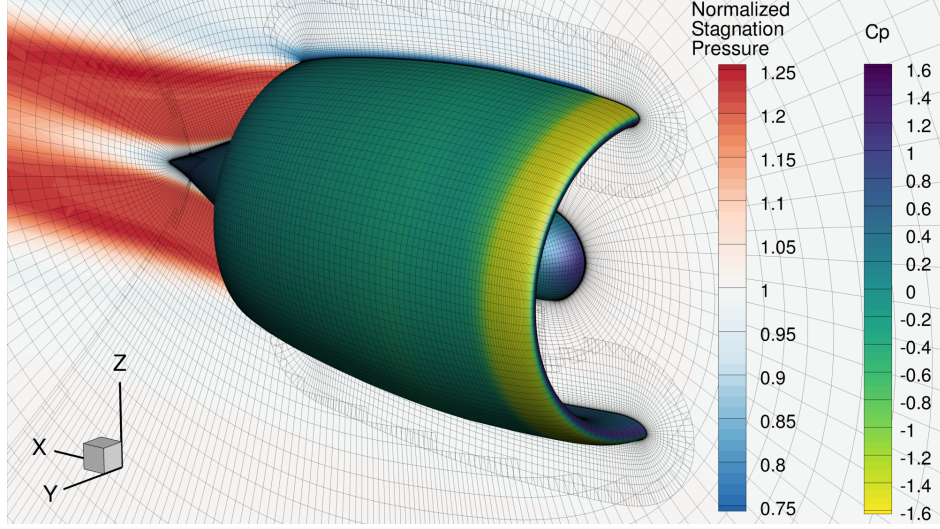


Figure 3: CFD solution of the podded fan.

condition for each design. For both the BLI and reference podded configurations, we use an actuator zone to model the effect of the fan on the flow.

Force accounting in a configuration that uses BLI is not straightforward; one must account for the pressure, viscous, and momentum based force terms along every solid surface. Due to these complications, instead of separating out the effects of the propulsor for both configurations, we use the net force coefficient in the  $x$  direction as the main force metric herein, which can be calculated as:

$$C_{f_x} = \frac{2}{\rho_\infty V_\infty^2 A_{\text{ref}}} \left[ \iint_S \left( (p - p_\infty) \hat{n} + \vec{f}_{\text{visc}} \right) \cdot \hat{e}_x dS + \vec{F}_{\text{fan}} \cdot \hat{e}_x \right], \quad (2)$$

where  $\hat{e}_x$  denotes the unit vector in the  $x$  direction of the aircraft frame of reference. This approach avoids the difficulties of using traditional thrust and drag accounting schemes with BLI because it does not require separating the effects of the propulsion system from the airframe. For the STARC-ABL concept the reference area  $A_{\text{ref}}$  is  $105.8\text{m}^2$ . The reference density  $\rho_\infty$  is  $0.3506\text{kg/m}^3$  and velocity  $V_\infty$  is  $231.7\text{m/s}$  at cruise conditions of Mach number (MN) 0.785 and altitude 37 000 ft. With this formulation, a positive  $C_{f_x}$  value means that there is a total net drag on the body, and this number represents the additional thrust required from the under-wing engines for the full configuration at steady flight, as we do not model the under-wing engines in this work.

For the podded configuration, we sum the results from the net force integrations of the podded propulsor (Fig. 3) and the non-BLI configuration (bottom half of Fig. 2). As a result, when both the BLI and podded configurations are optimized to the same net force coefficient target, the combined net force on the podded fan and non-BLI configuration is equal to the net force on the BLI configuration. With this approach, the shaft power for the BLI and podded configurations can be used to compute the PSC metric introduced in Eq. 1.

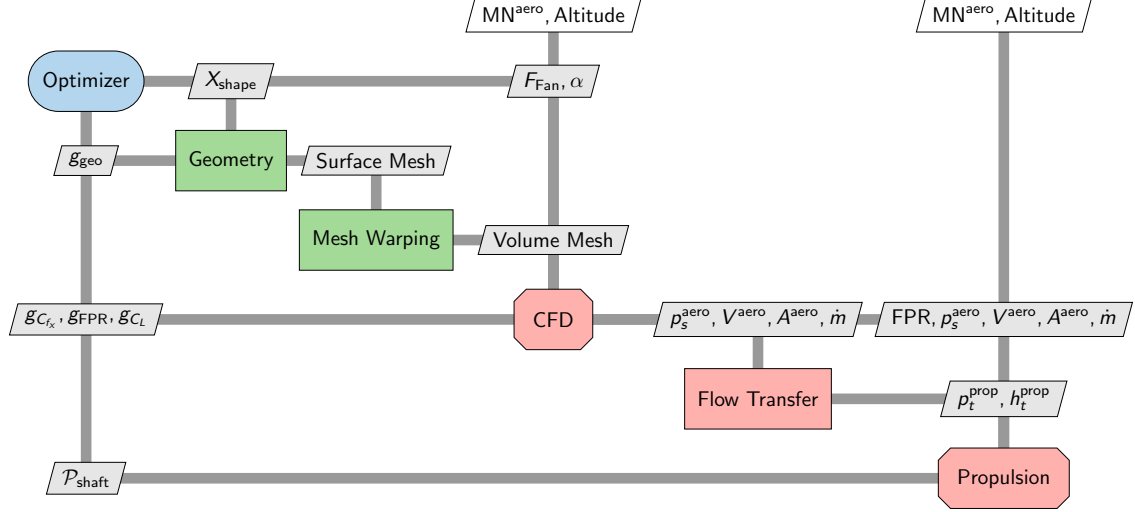


Figure 4: Coupled aeropropulsive design framework used to optimize the STARC-ABL configurations. In this representation, the optimizer is shown in blue, and the explicit and implicit components of the model are shown in green and red, respectively. The octagon shape is used to represent analysis groups consisting of multiple components.

Besides the CFD model, we also use a propulsion model to compute the power requirements to operate the BLI fan, because the RANS CFD model uses isentropic relationships which do not account for non-ideal losses in the fan. To accurately compute the power requirements of the fan, we use a 1-D propulsion model built with the pyCycle package [16]. This model uses the integrated quantities obtained from the CFD model to compute the power requirements of the BLI fan. To accurately transfer integrated total quantities from the CFD solver to be used in the propulsion model, we use the force-based averaging scheme developed by Gray et al. [20]. The extended design structure matrix (XDSM) diagram [21] of the resulting aeropropulsive design framework is shown in Figure 4.

### 3 Optimized STARC-ABL Designs

In previous work [12], we optimized the BLI and reference podded configurations at a combination of 3 net force and 3 FPR values, for a total of 18 optimized designs. The off-design analyses, which are the main focus of this paper, are performed using these optimized designs, and we summarize the results from the previous optimization study in the following sections.

#### 3.1 Optimization Problem Formulation

In the optimization problems, we minimize the shaft power required to achieve a specified net force on the entire body for each configuration. For the models used herein, “the entire body” includes the fuselage, vertical tail, wings, and aft propulsor (either in BLI or podded form), but does not include the under-wing engines. Therefore,

Table 1: Optimization problem definition. The podded configuration optimizations do not include the aft-fuselage design variables ( $x_{\text{fuse}}$ ).

	Variable/Function	Description	Quantity
minimize	$\mathcal{P}_{\text{shaft}}$	Shaft power required for the fan	1
with respect to	$\alpha$	Angle of attack	1
	$F_{\text{fan}}$	Body force applied to the fan	1
	$x_{\text{nacelle}}$	Fan nacelle shape	15
	$x_{\text{plug}}$	Fan plug shape	2
	$x_{\text{fuse}}$	Aft-fuselage shape	2
	Total		21
subject to	$C_{f_x} = C_{f_x}^*$	Target force coefficient	1
	$\text{FPR} = \text{FPR}^*$	Target FPR	1
	$C_L = 0.5$	Lift coefficient at cruise	1
	$0.99 < g_{\text{geo}} < 3.0$	Geometric thickness constraints	10
	Total		13

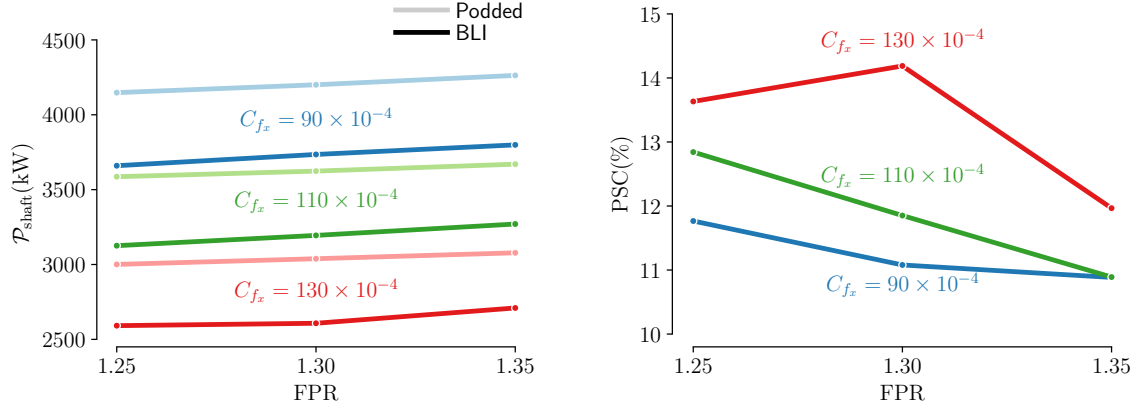
the net force target used in a given optimization can be seen as a *thrust deficit*. For steady flight, the amount of thrust required from the under-wing engines is equal to the net force target, or equivalently, proportional to the  $C_{f_x}$  value introduced in Equation 2. A lower  $C_{f_x}$  target is equivalent to having a smaller portion of the total thrust from the under-wing engines and a larger portion from the aft propulsor, which would mean a larger aft propulsor. Conversely, a larger  $C_{f_x}$  value represents designs where the under-wing engines need to provide more thrust, which would mean a smaller aft propulsor.

In these optimizations, the target values for  $C_{f_x}$  are  $90 \times 10^{-4}$ ,  $110 \times 10^{-4}$ , and  $130 \times 10^{-4}$ , while the target FPR values are 1.25, 1.30, and 1.35. Using these targets, the optimization problems we solved are summarized in Table 1. In these optimizations, we modify the geometry of the BLI fan nacelle and core using a number of sections, subject to geometric thickness constraints  $g_{\text{geo}}$  that are defined across the nacelle geometry to preserve the initial thickness. We use SNOPT [22] as the optimizer for these optimization problems, through the Python interface pyOptSparse [23], which is developed based on pyOpt [24].<sup>6</sup>

## 3.2 Optimization Results

All optimizations either converged successfully or terminated due to numerical difficulties after obtaining a feasible design, where the constraints were satisfied to a feasibility tolerance of  $10^{-4}$ . The shaft-power requirements for the BLI and podded configurations resulting from these optimization problems are shown in Figure 5a. Across the design space of net force and FPR, the BLI configuration requires less shaft power than the podded configuration to obtain the same net force on the whole aircraft. The opti-

<sup>6</sup><https://github.com/mdolab/pyoptsparse>, accessed November 2020



(a) Required shaft power for optimized results. (b) PSC values across the design space of net force and FPR.

Figure 5: Results from the optimization study performed by Yildirim et al. [12].

mized designs show that the shaft power required to operate the BLI fan increases with increasing FPR. Similarly, more power is required to operate the BLI fan for designs where a larger portion of the total thrust is obtained from it, which is equivalent to having a lower  $C_{fx}$  value.

Using these results, we compute PSC values across the design space of net force and FPR, which are shown in Figure 5b. The PSC results show two general trends. First of all, PSC values decrease as FPR increases. Secondly, designs with smaller BLI fans (i.e., higher  $C_{fx}$ ) get a higher PSC value, meaning that smaller fans benefit more from BLI. However, this does not mean that smaller fans would yield a better design overall. At the system level, it might be more beneficial to use a larger fan with a lower PSC value, rather than a smaller fan with a higher PSC value. This is because PSC values quantify the relative benefit that comes from BLI for a particular design. As a result, even though the large fans have lower PSC values, because the configuration would need less thrust from the under-wing engines, these designs might yield larger absolute power savings. Finally, the  $C_{fx} = 130 \times 10^{-4}$  and FPR = 1.30 design obtained a higher PSC value compared to the trend with the other  $C_{fx}$  values; this is due to the BLI design at this point obtaining a lower shaft power compared to the trend.

Figures 6 and 7 present the normalized stagnation pressure contours at the symmetry plane with the optimized designs of the BLI and podded configurations respectively. In these figures, we plot the areas where the total pressure is higher than the freestream total pressure with red, while areas that have a lower total pressure are highlighted with blue. This color map demonstrates the effects caused by the wake of the fuselage and the power added to the flow by the BLI and podded fans.



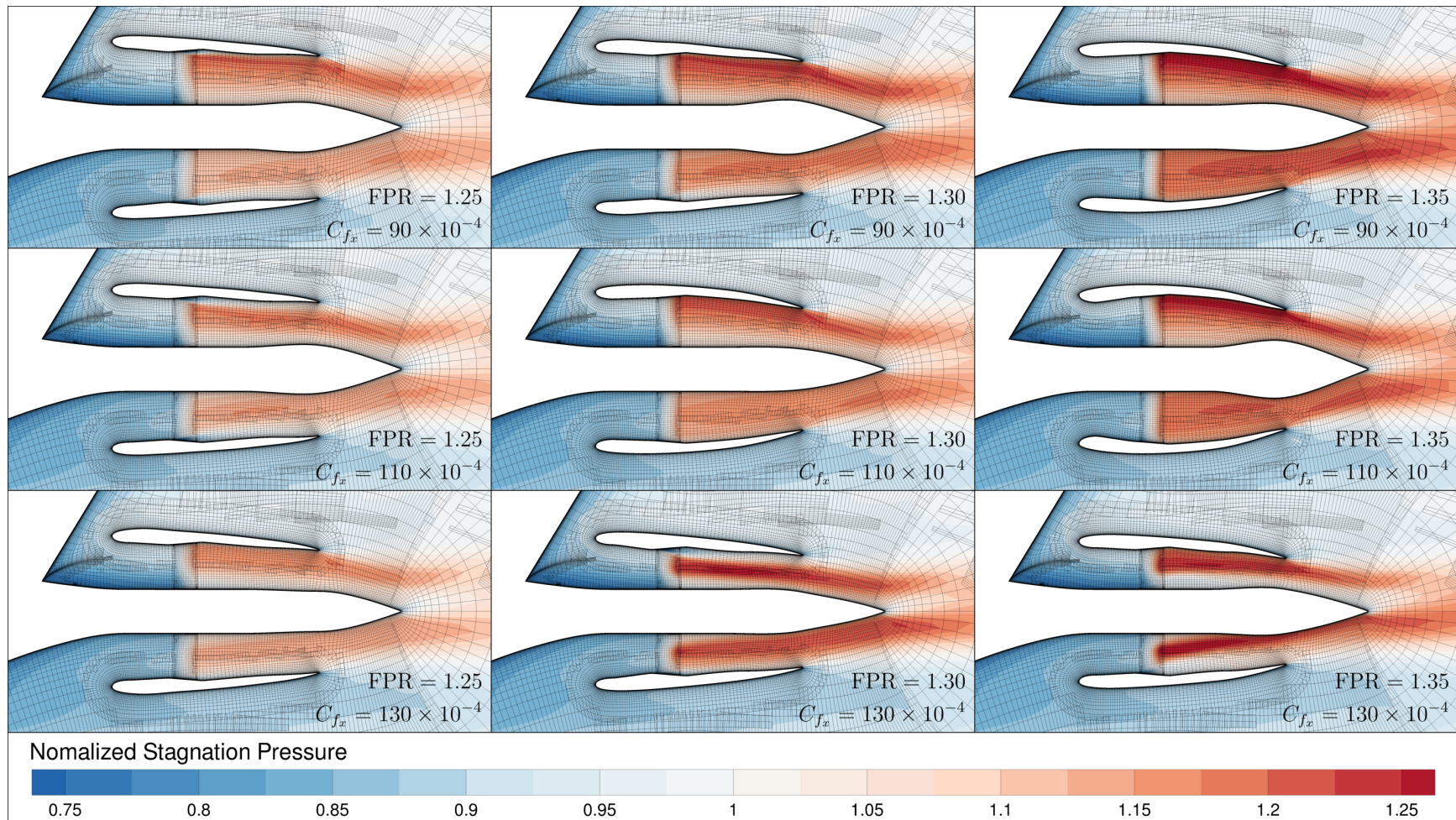


Figure 6: Normalized stagnation pressure contours with the optimized BLI configurations.



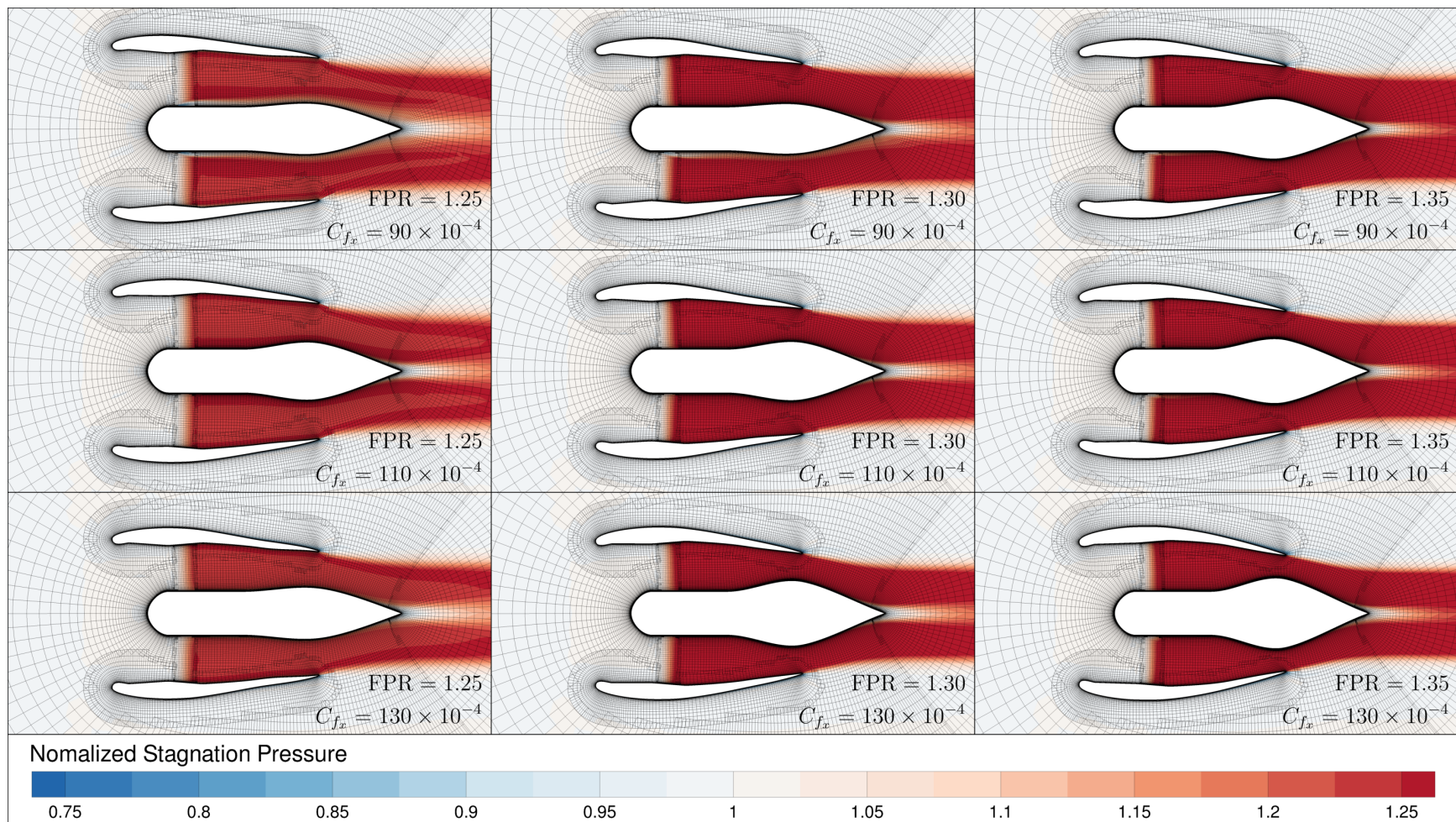


Figure 7: Normalized stagnation pressure contours with the optimized podded configurations.

## 4 Off-Design Analysis Approach

While the PSC results presented in Figure 5b are useful to study the benefit of BLI at cruise conditions, these values do not represent the total benefit of BLI to these configurations. This is primarily because the mission profile of an aircraft of this size includes multiple important flight conditions. The benefit of BLI must be computed across all of these points to compute the total advantage accurately. Furthermore, due to the low design FPR values and because it is electrically powered, the aft-propulsor design of the STARC-ABL concept has unique challenges in low-altitude and low-speed flight conditions. Therefore, it is vital to develop a method to analyze the aeropropulsive performance at these off-design conditions.

The distinction of on- and off-design analysis points arise from how the propulsion system is modeled, as explained by Hendricks and Gray [16]. The on-design (or design for short) case is the single flight condition where we adjust the fan model’s parameters. For our case, the design point is the cruise condition that we use to optimize the BLI and podded configurations. Once the fan model parameters are set using the design point, we can then perform off-design analyses, where the performance of the same fan design can be obtained at flight conditions other than cruise. However, while the on- and off-design analysis approaches are well defined for standalone propulsion models, we need to develop a new approach to quantify the benefits of BLI at off-design conditions using coupled aeropropulsive models.

The objective of these off-design analyses is to accurately model the aeropropulsive benefit of BLI across a range of flight conditions, and this results in several requirements: First of all, the BLI and podded configurations must be analyzed at the same net force because we are using the PSC formulation (Eq. 1) as the primary metric to measure BLI benefit. We control these net force values at off-design conditions by changing how much thrust is applied in the CFD model’s actuator zone. This parameter is a design variable in the optimizations (see Section 3), and the optimized value is selected to match the target FPR and net force at cruise conditions. However, at off-design flight conditions, we need to select a new thrust value for both BLI and podded configurations. This value controls how much momentum is added to the fan model’s flow in the CFD simulation. Even though it is not equal to the total force (see Eq. 2), we can use it to control the total force on the BLI and podded configurations.

Secondly, we assume that the electric motor and the power transmission system that drives the aft-propulsor are sized during cruise conditions. Therefore, this system can only supply up to the shaft power at cruise conditions regardless of the flight condition. Furthermore, we assume that the BLI benefits will be largest when the BLI fan operates at maximum power. We analyze the aft-propulsor with the BLI configuration at the shaft-power value used for the cruise condition because of these assumptions.

Finally, we must have the FPR values match between the CFD simulation and the propulsion model to have a consistent aeropropulsive model. This is because the FPR values at these off-design conditions can be much lower than the design values, significantly affecting the fan’s efficiency. We adjust the fan model’s rotation speed to vary the FPR value in the propulsion model until it matches the value obtained from the CFD model. Matching this parameter between the two models ensures that

we obtain a consistent result, even though the CFD model does not include non-ideal losses.

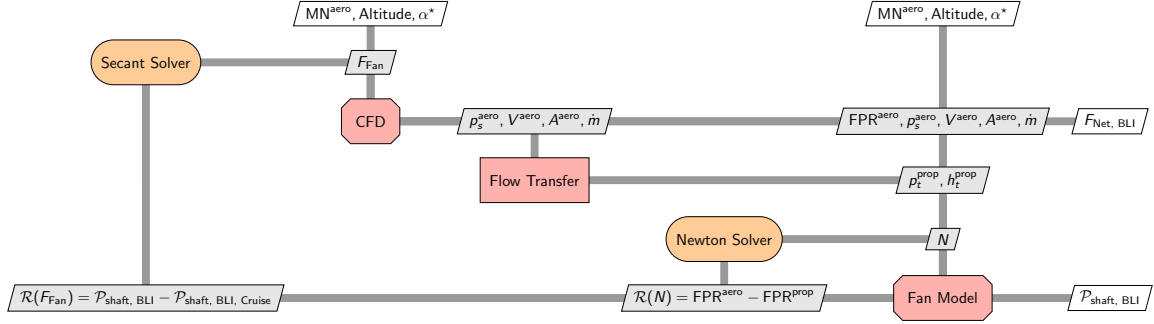
With these requirements in mind, we define the steps required to obtain PSC values at off-design analysis points. The steps we follow to compute the PSC values at off-design flight conditions are as follows:

1. We first simulate the BLI configuration at the off-design conditions using the model layout shown in Figure 8a. In this step, we adjust the CFD fan model's thrust until the propulsion model's shaft power matches the shaft power at cruise conditions. We also adjust the fan model's rotation speed to match the FPR value of the propulsion model to the FPR value from the CFD simulation. Once the shaft power and FPR output from the propulsion model converges to the target values, we record the net force on the whole body from the CFD simulation and use it in the next step.
2. Following the BLI configuration simulation, we simulate the podded configuration at the same net force result from the previous step, as shown in Figure 8b. We meet this net force target by modifying the thrust applied in the CFD fan model. Similar to the previous step, we also adjust the fan model's rotation speed to match the propulsion model's FPR value to the FPR value from the CFD simulation. Once the CFD model's net force and the FPR value from the propulsion model match the target values, we record the propulsion model's shaft-power requirement and move to the next step.
3. In the final step, we use the shaft-power results from the previous two steps to compute the PSC values as defined in Equation 1. Because we selected to operate the BLI fan at the design shaft-power in these off-design conditions, any change in the PSC values is caused by the changes in the podded configuration's shaft-power requirements. Even though the shaft-power requirement of the BLI configuration does not change at these off-design conditions, the use of BLI affects the total net force on the aircraft. This value is then used in the podded configurations to obtain the shaft-power requirements at the same net force values.

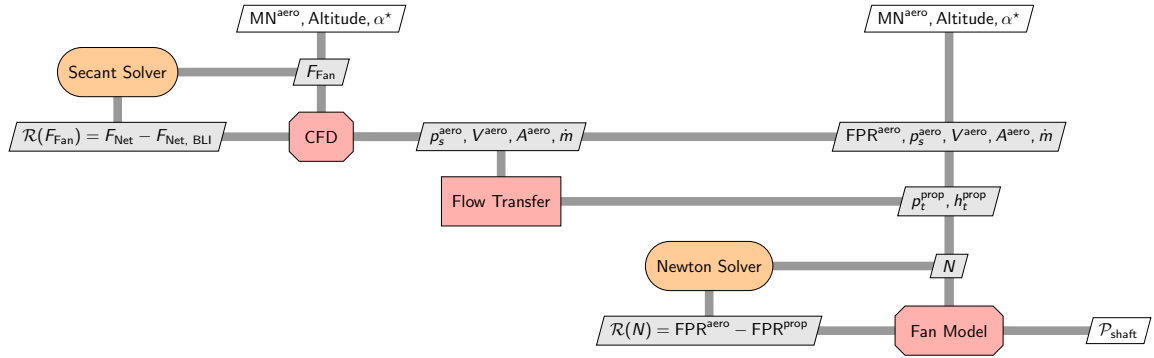
This approach satisfies all three requirements we listed above. It is consistent with the on-design analysis approach we use with the design optimizations; utilizing this methodology to analyze the cruise PSC values gives the same PSC values compared to performing an on-design analysis approach for cruise conditions. While we can use the same model structure for the optimization of the BLI and podded configurations (Fig. 4), the model structure used for the two configurations are different for off-design analyses, as shown in Figures 8a and 8b. This is because the CFD fan model thrust is determined at different targets for each configuration; the BLI configuration is analyzed at a target shaft power, while the podded configuration is analyzed at a target net force.

This off-design approach results in running 19 analyses to compute the PSC values at each additional flight condition. This is because we have 9 optimized designs for both BLI and podded configurations; however, the design of the non-BLI airframe shown in the bottom half of Figure 2 is not modified during the design optimizations, and is the





(a) XDSM diagram for the off-design analysis model structure used for the BLI configuration. The top-level secant solver changes the thrust applied at the actuator zone ( $\mathbf{F}_{Fan}$ ) until the shaft power from the propulsion model is equal to the design shaft power for the BLI propulsor. The Newton solver adjusts the rotation speed ( $\mathbf{N}$ ) of the fan model to match the FPR of the propulsion model to the FPR value obtained by the CFD model. The final solution is obtained when these two residuals ( $\mathcal{R}(\mathbf{F}_{Fan})$ ,  $\mathcal{R}(\mathbf{N})$ ) are converged to zero. We record the net force on the BLI configuration ( $\mathbf{F}_{Net, BLI}$ ) to be used as the net force target for the podded configuration analysis shown in Figure 8b.



(b) XDSM diagram for the off-design analysis model structure used for the podded configuration. The top-level secant solver changes the thrust applied at the actuator zone ( $\mathbf{F}_{Fan}$ ) until the net force on the podded configuration matches the net force result from the BLI configuration shown in Figure 8a. This approach ensures that the two configurations are analyzed at the same net force value, as required by the PSC formulation (Eq. 1). The Newton solver adjusts the rotation speed ( $\mathbf{N}$ ) of the fan model to match the FPR of the propulsion model to the FPR value obtained by the CFD model. The final solution is obtained when these two residuals ( $\mathcal{R}(\mathbf{F}_{Fan})$ ,  $\mathcal{R}(\mathbf{N})$ ) are converged to zero, and finally, we can compute the PSC value using the shaft-power requirements of the BLI and podded configurations.

Figure 8: XDSM diagrams for the model structures used in the off-design analyses. We first analyze the BLI configuration using the formulation in Figure 8a, and then use the resulting net power value ( $\mathbf{F}_{Net, BLI}$ ) in the analysis of the podded configuration with the formulation in Figure 8b. At each flight condition, we specify the altitude, MN, and angle of attack ( $\alpha^*$ ) that is required to match the  $\mathbf{C}_L$  target listed in Table 2.

same across all podded designs. Therefore, we only need to simulate this mesh once per flight condition to obtain the net force, which is then added together with the net force from simulations of the podded fan mesh (Figure 3). As a result, each additional flight conditions requires simulations of 9 BLI designs, 9 podded fan designs, and 1 non-bli configuration, resulting in a total of 19 analyses per flight condition.

Using this approach, we analyzed the off-design performance of 8 additional flight conditions, as listed in Table 2 along with the cruise condition of the STARC-ABL concept. As a result, computing the PSC values across these 9 flight conditions require results from 171 coupled aeropropulsive simulations. These flight conditions are selected to represent important flight conditions like take-off and approach, as well as to quantify the sensitivity of the PSC values to changes in altitude, MN, and lift coefficient.

Table 2: The 9 flight conditions we used to compute the PSC values. The first analysis condition represents take-off at zero degrees angle of attack (AoA), while the rest of the conditions are analyzed at the target lift coefficients listed. The last flight condition listed is the cruise conditions used for the design optimizations.

Flight Conditions	Altitude (ft)	MN	$C_L$
Take-off	0	0.2	at 0° AoA
Approach	1 000	0.2	0.5
	1 000	0.2	1.0
	1 000	0.3	0.5
	6 000	0.3	0.5
Hold	15 000	0.5	0.3
	15 000	0.5	0.5
	15 000	0.5	0.7
Cruise	37 000	0.785	0.5

## 5 Results

Using the off-design analysis method described in the previous section, we analyzed the aeropropulsive performance of 18 optimized designs at 9 flight conditions listed in Table 2 and used this data to compute the PSC values of 9 design points at 8 off-design conditions, along with cruise conditions. In this section, we present the PSC trends at these flight conditions using the optimized designs at  $C_{fx} = 110 \times 10^{-4}$  and FPR values of 1.25, 1.30, and 1.35. For brevity, the full set of PSC data at all flight conditions using all designs is listed in Appendix A.

In the following figures, we plot the PSC values at specified flight conditions with respect to the design FPR for simplicity. This design FPR is the target FPR value used in the optimizations. At the off-design conditions analyzed herein, the actual FPR values at each analysis point are likely to be much lower than the design targets of FPR values. This is because we perform the off-design analyses by matching the

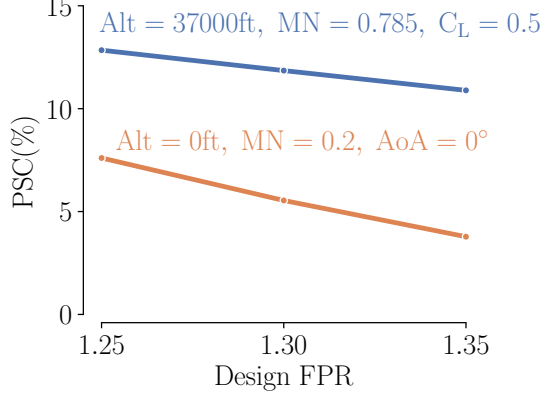
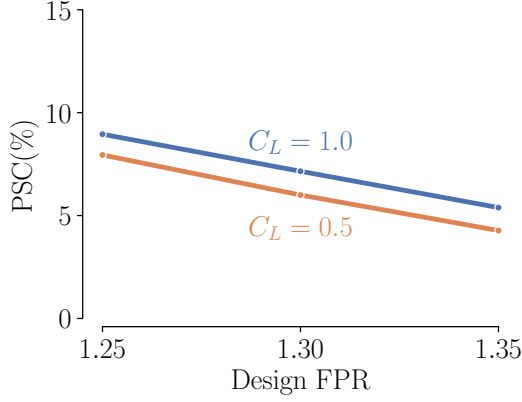


Figure 9: PSC values of  $\mathbf{C}_{fx} = 110 \times 10^{-4}$  designs at cruise (blue) and take-off (orange) conditions. The cruise conditions represent the on-design PSC values, and the take-off conditions represent the lower end of PSC values, where the benefit of BLI is the smallest across the flight conditions we analyzed herein.

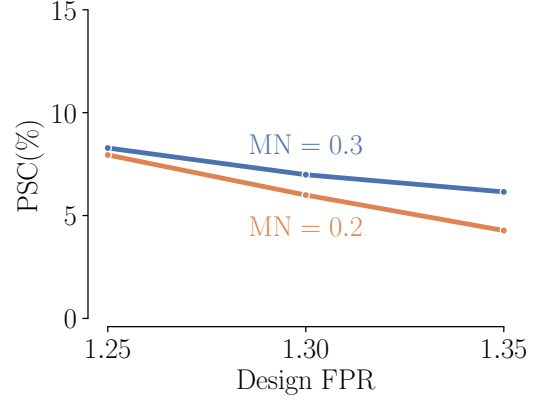
off-design shaft-power requirement to the cruise shaft power rather than matching the off-design FPR to the design FPR. As a result, these plots' horizontal axis shows the design FPR values to demonstrate better how much the PSC values change for each design at various flight conditions.

One of this study's primary goals is to quantify how the PSC values change at various flight conditions compared to the cruise condition used for optimizing the BLI and podded configurations. First of all, we compare the two extreme conditions: cruise and take-off, which represent the two extreme speed and altitude cases among the flight conditions we consider in this work. Figure 9 shows the PSC values at cruise and take-off using the optimized designs at  $C_{fx} = 110 \times 10^{-4}$  and FPR values of 1.25, 1.30, and 1.35. The PSC values dropped across all design FPR values, while the higher FPR designs were affected more by the lower speed and altitude. The PSC value of the design FPR 1.25 case dropped from 12.8% to 7.6%, while the design FPR 1.35 case dropped from 10.9% to 3.5%. This is a drastic change in PSC values; however, the PSC values during take-off conditions are the lowest among the flight conditions we studied herein, and therefore, this change represents the largest drop in PSC. In contrast, every other flight condition obtained a PSC value between the cruise and take-off conditions.

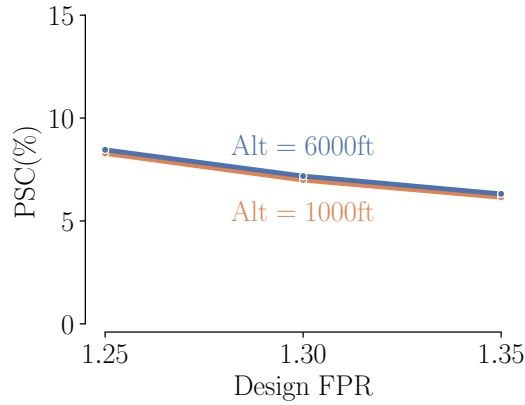
Secondly, we study the sensitivity of PSC values to  $C_L$ , MN, and altitude about low-speed and low-altitude flight conditions. Figure 10a shows the PSC values for two flight conditions at an altitude of 1000 ft and MN of 0.2, with different  $C_L$  values of 0.5, and 1.0. These results show that increasing  $C_L$  from 0.5 to 1.0 at this flight condition increases PSC values uniformly across all 3 design FPR points by about 1 percentage point. Figure 10b shows the effect of perturbing the MN at an altitude of 1000 ft and  $C_L$  of 0.5. For this case, increasing the MN from 0.2 to 0.3 increased the PSC value of the 1.25 design FPR case by 0.3%, while the PSC of the 1.35 design FPR case by 1.9%. This shows that the PSC values for higher design FPR cases are more sensitive to changes in MN, compared to lower design FPR cases. Finally, Figure 10c shows the effect of increasing the altitude from 1000 ft to 6000 ft at a MN of 0.3 and  $C_L$  of 0.5.



(a) PSC results from two flight conditions at an altitude of 1000 feet and MN of 0.2. The PSC values increase uniformly across all FPR values with increasing  $C_L$ .



(b) PSC results from two flight conditions at an altitude of 1000 feet and  $C_L$  of 0.5. The PSC values increase with increasing MN; however, PSC values of higher FPR designs are more sensitive to changes in MN compared to lower FPR designs.



(c) PSC results from two flight conditions at a MN of 0.3 and  $C_L$  of 0.5. The PSC values increase slightly with increasing altitude, but the effects are smaller compared to the sensitivity of PSC to  $C_L$  or MN.

Figure 10: Results from low speed and low altitude flight conditions that visualize the trends in PSC using the designs optimized at  $C_{fx} = 110 \times 10^{-4}$ .

These results show that the PSC values are not very sensitive to altitude changes; an increase of 5000 ft in altitude resulted in less than 0.2% increase in PSC values across all design FPR cases.

The last set of cases we study are at an altitude of 15000 ft and MN of 0.5, with  $C_L$  values of 0.3, 0.5, and 0.7, as shown in Figure 11. These results show that the PSC values increase by about 1% across all design FPR cases with an increase of 0.2 in  $C_L$ , and this is similar to the trend shown in Figure 10a. The fact that the PSC values still increase at  $C_L$  values that are larger than the 0.5 value used in the optimizations shows



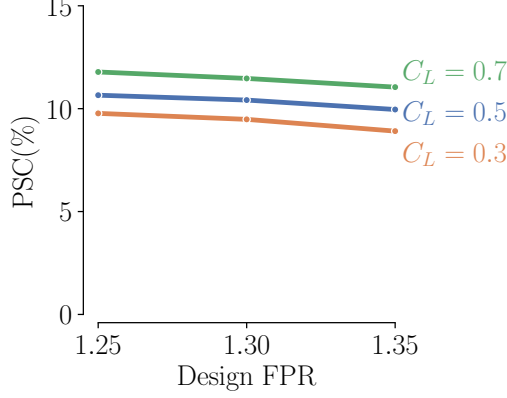


Figure 11: PSC results from three flight conditions at an altitude of 15 000 ft and MN of 0.5 using the designs optimized at  $\mathbf{C}_{f_x} = 110 \times 10^{-4}$ . The PSC values uniformly increase with increasing  $\mathbf{C}_L$ , and this trend holds true for  $\mathbf{C}_L$  values higher than the design  $\mathbf{C}_L$  of 0.5, demonstrating that adjusting the lift distribution during design optimization can lead to higher PSC values.

that the BLI benefit does increase with increasing  $C_L$ . This can be explained by either the BLI fan performing better with more downwash, the podded fan performing worse with a higher angle of attack, or both. Regardless of the reason for this trend, it creates an interesting tradeoff between lift distribution and aeropropulsive performance. In the design optimizations we used herein, we used the same wing design for both the BLI and non-BLI configurations. Therefore, the two configurations had the same span-wise lift distribution. However, this trend suggests that optimizing the wing design and the aeropropulsive design of the BLI fan can lead to more considerable aeropropulsive benefits, and the optimal lift distribution for the two configurations can differ. While it can be more beneficial for the BLI configuration to have more lift inboard to increase BLI benefits, the podded configuration is more likely to obtain a better lift distribution for reducing the induced drag. This tradeoff further shows the importance of using aeropropulsive design optimization with configurations that use BLI due to the tight integration of the propulsion system with the airframe.

## 6 Conclusions

The STARC-ABL configuration introduced by NASA utilizes BLI technology on a conventional airframe. While previous work from authors explored the benefits of BLI to this configuration at cruise conditions, the performance impact of the BLI system was not studied at low-speed and low-altitude flight conditions. In this work, we analyzed the benefit of BLI on the STARC-ABL configuration across a range of flight conditions to quantify the benefit of BLI across the mission profile.

The results show that while the PSC values are around 10 to 15% for the cruise conditions, they drop significantly at low-speed and low-altitude conditions like take-off. Furthermore, we studied the sensitivity of PSC values to changes in altitude, MN, and  $C_L$  at off-design flight conditions. These results show that the PSC values uniformly

increase with increasing  $C_L$ . Besides this, a higher MN results in higher PSC values, while this trend is less pronounced in lower-FPR designs. Finally, altitude does not strongly affect PSC values about the flight conditions we analyzed. The sensitivity of PSC to  $C_L$  creates a complex tradeoff between lift distribution and aeropropulsive performance. This result further enforces that high-fidelity aeropropulsive design optimization is required to integrate these emerging propulsion technologies into the airframe.

In future work, we will focus on the development of a tightly-coupled aeropropulsive modeling approach. The off-design analyses show that while the non-ideal losses are small relative to the differences in shaft power between BLI and podded configurations at cruise conditions, these losses can become significant at low-speed and low-altitude flight conditions. Furthermore, the lower PSC values at these off-design points make the PSC computation more sensitive to the changes in shaft-power requirements for both configurations. Therefore, to accurately analyze the aeropropulsive performance at off-design flight conditions, we will include thermal losses from the propulsion model in the CFD model as heat addition.

## Acknowledgments

This work was funded by the NASA Advanced Air Transport Technology (AATT) and Transformational Tools and Technologies (TTT) projects.

## References

- [1] David K. Hall, Arthur C. Huang, Alejandra Uranga, Edward M. Greitzer, Mark Drela, and Sho Sato. Boundary layer ingestion propulsion benefit for transport aircraft. *Journal of Propulsion and Power*, 33(5):1118–1129, 2017. doi:[10.2514/1.B36321](https://doi.org/10.2514/1.B36321).
- [2] P. Laskaridis, V. Pachidis, and P. Pilidis. Opportunities and challenges for distributed propulsion and boundary layer ingestion. *Aircraft Engineering and Aerospace Technology*, 86(6):451–458, 2014. doi:[10.1108/AEAT-05-2014-0067](https://doi.org/10.1108/AEAT-05-2014-0067).
- [3] Alejandra Uranga, Mark Drela, David K. Hall, and Edward M. Greitzer. Analysis of the Aerodynamic Benefit from Boundary Layer Ingestion for Transport Aircraft. *AIAA Journal*, 0(0):1–11, 2018. ISSN 0001-1452. doi:[10.2514/1.J056781](https://doi.org/10.2514/1.J056781).
- [4] A. L. Habermann, J. Bijewitz, A. Seitz, and M. Hornung. Performance bookkeeping for aircraft configurations with fuselage wake-filling propulsion integration. *CEAS Aeronautical Journal*, December 2019. ISSN 1869-5590. doi:[10.1007/s13272-019-00434-w](https://doi.org/10.1007/s13272-019-00434-w).
- [5] Eric S. Hendricks. A review of boundary layer ingestion modeling approaches for use in conceptual design. Technical report, July 2018. URL <https://ntrs.nasa.gov/search.jsp?R=20180005165>.

- [6] Luca Menegozzo and Ernesto Benini. Boundary layer ingestion propulsion: A review on numerical modeling. *Journal of Engineering for Gas Turbines and Power*, 142(12):120801, December 2020. ISSN 0742-4795, 1528-8919. doi:[10.1115/1.4048174](https://doi.org/10.1115/1.4048174).
- [7] Jr. Smith, Leroy. Wake ingestion propulsion benefit. In *27th Joint Propulsion Conference*, Joint Propulsion Conferences. American Institute of Aeronautics and Astronautics, June 1991. doi:[10.2514/6.1991-2007](https://doi.org/10.2514/6.1991-2007).
- [8] Mark Drela. Power Balance in Aerodynamic Flows. *AIAA Journal*, 47(7):1761–1771, July 2009. ISSN 0001-1452. doi:[10.2514/1.42409](https://doi.org/10.2514/1.42409).
- [9] Jason Welstead and James L. Felder. Conceptual Design of a Single-Aisle Turbo-electric Commercial Transport with Fuselage Boundary Layer Ingestion. In *54th AIAA Aerospace Sciences Meeting*, AIAA SciTech Forum. American Institute of Aeronautics and Astronautics, January 2016. doi:[10.2514/6.2016-1027](https://doi.org/10.2514/6.2016-1027).
- [10] Justin S. Gray, Charles A. Mader, Gaetan K. W. Kenway, and Joaquim R. R. A. Martins. Coupled aeropropulsive design optimization of a three-dimensional BLI propulsor considering inlet distortion. *Journal of Aircraft*, 2020. doi:[10.2514/1.C035845](https://doi.org/10.2514/1.C035845).
- [11] Anil Yildirim, Justin S. Gray, Charles A. Mader, and Joaquim R. R. A. Martins. Aeropropulsive design optimization of a boundary layer ingestion system. In *AIAA Aviation Forum*, Dallas, TX, June 2019. doi:[10.2514/6.2019-3455](https://doi.org/10.2514/6.2019-3455).
- [12] Anil Yildirim, Justin S. Gray, Charles A. Mader, and J. R. R. A. Martins. Boundary layer ingestion benefit for the STARC-ABL configuration. *Journal of Aircraft*, 2020. (Submitted).
- [13] Andrew Hahn. Vehicle sketch pad: A parametric geometry modeler for conceptual aircraft design. In *48th AIAA Aerospace Sciences Meeting Including the New Horizons Forum and Aerospace Exposition*, Aerospace Sciences Meetings. American Institute of Aeronautics and Astronautics, January 2010. doi:[10.2514/6.2010-657](https://doi.org/10.2514/6.2010-657).
- [14] Ney Secco, Gaetan K. W. Kenway, Ping He, Charles A. Mader, and Joaquim R. R. A. Martins. Efficient mesh generation and deformation for aerodynamic shape optimization. *AIAA Journal*, 2020. (In press).
- [15] Charles A. Mader, Gaetan K. W. Kenway, Anil Yildirim, and Joaquim R. R. A. Martins. ADflow—an open-source computational fluid dynamics solver for aerodynamic and multidisciplinary optimization. *Journal of Aerospace Information Systems*, 2020. doi:[10.2514/1.1010796](https://doi.org/10.2514/1.1010796).
- [16] Eric S. Hendricks and Justin S. Gray. pycycle: A tool for efficient optimization of gas turbine engine cycles. *Aerospace*, 6(87), August 2019. doi:[10.3390/aerospace6080087](https://doi.org/10.3390/aerospace6080087).

- [17] Anil Yildirim, Gaetan K. W. Kenway, Charles A. Mader, and Joaquim R. R. A. Martins. A Jacobian-free approximate Newton–Krylov startup strategy for RANS simulations. *Journal of Computational Physics*, 397:108741, November 2019. ISSN 0021-9991. doi:[10.1016/j.jcp.2019.06.018](https://doi.org/10.1016/j.jcp.2019.06.018).
- [18] Gaetan K. W. Kenway, Charles A. Mader, Ping He, and Joaquim R. R. A. Martins. Effective adjoint approaches for computational fluid dynamics. *Progress in Aerospace Sciences*, 110:100542, October 2019. doi:[10.1016/j.paerosci.2019.05.002](https://doi.org/10.1016/j.paerosci.2019.05.002).
- [19] Justin S. Gray, John T. Hwang, Joaquim R. R. A. Martins, Kenneth T. Moore, and Bret A. Naylor. OpenMDAO: An open-source framework for multidisciplinary design, analysis, and optimization. *Structural and Multidisciplinary Optimization*, 59(4):1075–1104, April 2019. doi:[10.1007/s00158-019-02211-z](https://doi.org/10.1007/s00158-019-02211-z).
- [20] Justin S. Gray, Charles A. Mader, Gaetan K. W. Kenway, and Joaquim R. R. A. Martins. Modeling boundary layer ingestion using a coupled aeropropulsive analysis. *Journal of Aircraft*, 55(3):1191–1199, May 2018. doi:[10.2514/1.C034601](https://doi.org/10.2514/1.C034601).
- [21] Andrew B. Lambe and Joaquim R. R. A. Martins. Extensions to the design structure matrix for the description of multidisciplinary design, analysis, and optimization processes. *Structural and Multidisciplinary Optimization*, 46:273–284, August 2012. doi:[10.1007/s00158-012-0763-y](https://doi.org/10.1007/s00158-012-0763-y).
- [22] Philip E. Gill, Walter Murray, and Michael A. Saunders. SNOPT: An SQP algorithm for large-scale constrained optimization. *SIAM Journal of Optimization*, 12(4):979–1006, 2002. doi:[10.1137/S1052623499350013](https://doi.org/10.1137/S1052623499350013).
- [23] Neil Wu, Gaetan Kenway, Charles A. Mader, John Jasa, and Joaquim R. R. A. Martins. pyOptSparse: a Python framework for large-scale constrained nonlinear optimization of sparse systems. *Journal of Open Source Software*, 5(54):2564, October 2020. doi:[10.21105/joss.02564](https://doi.org/10.21105/joss.02564).
- [24] Ruben E. Perez, Peter W. Jansen, and Joaquim R. R. A. Martins. pyOpt: A Python-based object-oriented framework for nonlinear constrained optimization. *Structural and Multidisciplinary Optimization*, 45(1):101–118, January 2012. doi:[10.1007/s00158-011-0666-3](https://doi.org/10.1007/s00158-011-0666-3).

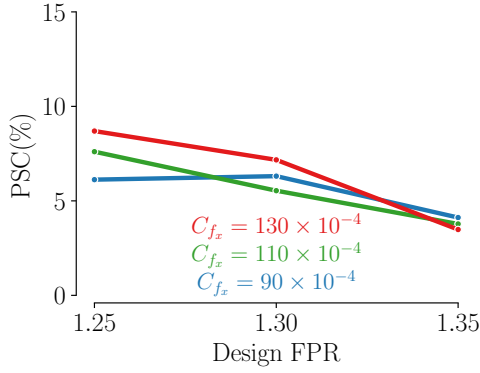


## A The Full Set of PSC Data

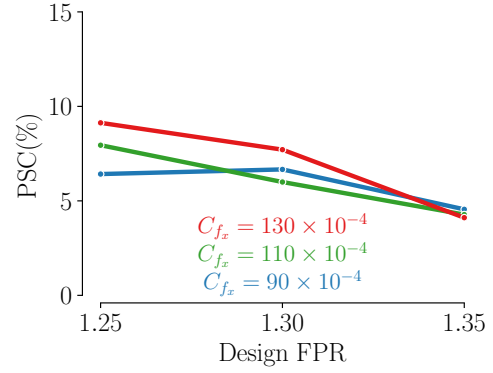
Figures 12a through 13c and Table 3 show the PSC data across all of the flight conditions listed in Table 2 using all of the optimized designs introduced in Section 3. As explained in Section 5, the horizontal axis in these plots show the design FPR, rather than the actual FPR result from these analyses. Similarly, the  $C_{fx}$  values listed represent the target  $C_{fx}$  values used in the optimized designs detailed in Section 3. This is done to better visualize the changes in PSC values for each optimization point compared to the design values. These results can be used to guide future estimations of total benefit of BLI on the STARC-ABL concept, as well as forming a baseline study for future aeropropulsive design optimization studies that involve off-design analysis conditions.

Table 3: PSC results in percentage points using all designs at all flight conditions.

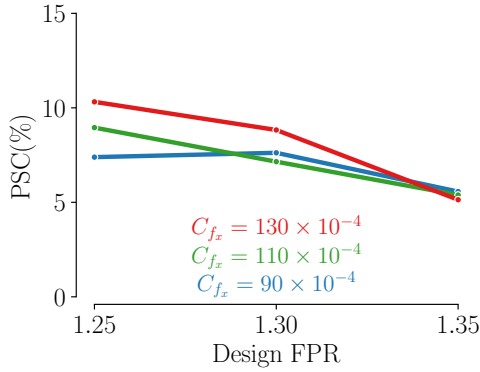
					$C_{fx}$		
					$90 \times 10^{-4}$	$110 \times 10^{-4}$	$130 \times 10^{-4}$
FPR	1.25	Alt (ft)	MN	$C_L$			
		0	0.2	at 0° AoA	6.12	7.60	8.69
		1 000	0.2	0.5	6.42	7.95	9.13
		1 000	0.2	1.0	7.39	8.95	10.32
		1 000	0.3	0.5	7.12	8.28	9.11
		6 000	0.3	0.5	7.09	8.46	9.31
		15 000	0.5	0.3	8.57	9.77	10.97
		15 000	0.5	0.5	9.38	10.65	11.89
		15 000	0.5	0.7	10.45	11.78	13.05
		37 000	0.785	0.5	11.77	12.84	13.63
	1.30	0	0.2	at 0° AoA	6.31	5.54	7.17
		1 000	0.2	0.5	6.66	6.00	7.71
		1 000	0.2	1.0	7.62	7.15	8.83
		1 000	0.3	0.5	7.46	6.99	8.20
		6 000	0.3	0.5	7.40	7.18	8.19
		15 000	0.5	0.3	8.96	9.48	10.93
		15 000	0.5	0.5	9.84	10.42	11.86
		15 000	0.5	0.7	10.86	11.47	12.95
		37 000	0.785	0.5	11.08	11.85	14.19
	1.35	0	0.2	at 0° AoA	4.12	3.78	3.48
		1 000	0.2	0.5	4.55	4.27	4.11
		1 000	0.2	1.0	5.57	5.39	5.14
		1 000	0.3	0.5	6.08	6.15	5.90
		6 000	0.3	0.5	6.27	6.31	5.95
		15 000	0.5	0.3	8.69	8.91	9.51
		15 000	0.5	0.5	9.60	9.96	10.49
		15 000	0.5	0.7	10.63	11.05	11.56
		37 000	0.785	0.5	10.88	10.89	11.97



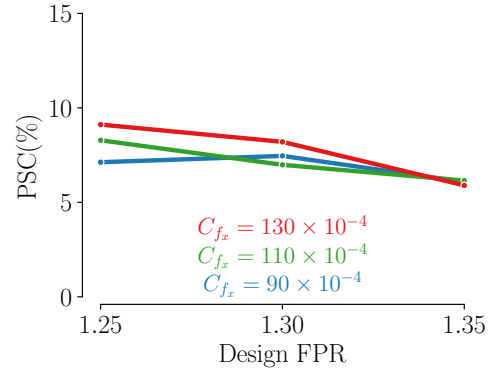
(a) Altitude 0 ft, MN 0.2, at  $0^\circ$  AoA



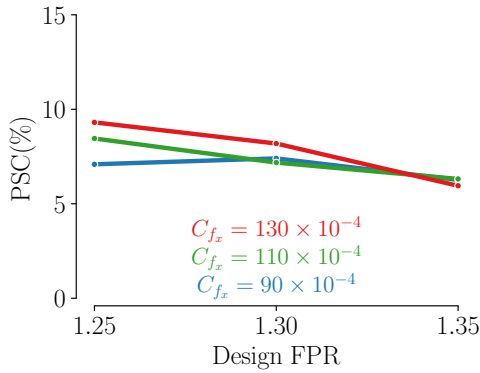
(b) Altitude 1000 ft, MN 0.2,  $C_L$  0.5



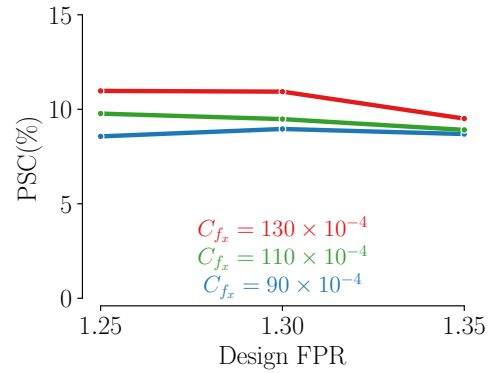
(c) Altitude 1000 ft, MN 0.2,  $C_L$  1.0



(d) Altitude 1000 ft, MN 0.3,  $C_L$  0.5

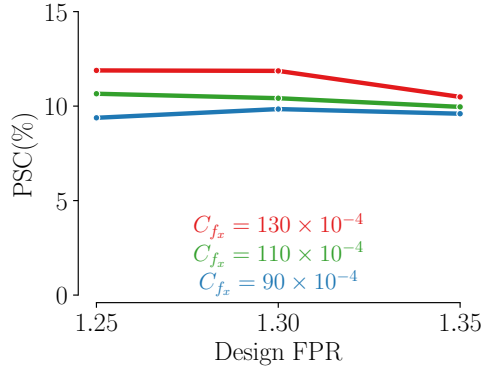


(e) Altitude 6000 ft, MN 0.3,  $C_L$  0.5

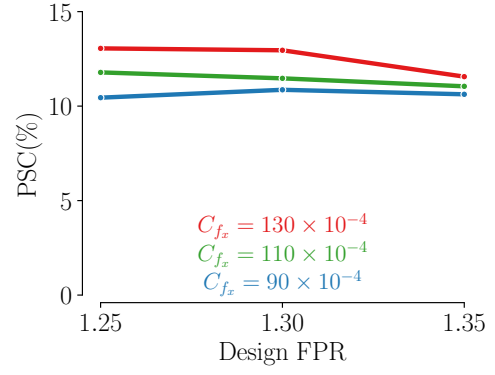


(f) Altitude 15000 ft, MN 0.5,  $C_L$  0.3

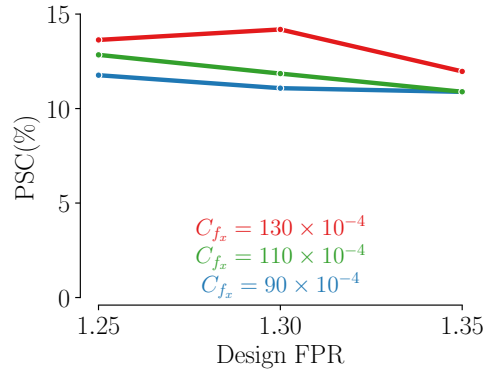
Figure 12: Full set of PSC data computed with 18 optimized designs across 9 flight conditions.



(a) Altitude 15 000 ft, MN 0.5,  $\mathbf{C_L}$  0.5



(b) Altitude 15 000 ft, MN 0.5,  $\mathbf{C_L}$  0.7



(c) Altitude 37 000 ft, MN 0.785,  $\mathbf{C_L}$  0.5

Figure 13: Full set of PSC data computed with 18 optimized designs across 9 flight conditions. (continued)